Influence of wettability on phase connectivity and electrical resistivity

Zhishang Liu,[1] James E. McClure,[2] and Ryan T. Armstrong[1,*]
[1]*School of Minerals and Energy Resources Engineering, University of New South Wales, Sydney 2052, Australia*
[2]*Advanced Research Computing, Virginia Tech, Blacksburg, Virginia 24061, USA*

(Received 2 April 2018; published 8 October 2018)

Experimental results have shown that resistivity index can deviate from Archie's law at low conductive phase saturation. Previous works have claimed that wettability and flow history are the two main factors causing this phenomenon. Herein, we investigate how the underlying fluid morphology influences electrical resistivity. We start from digital synchrotron x-ray microcomputed tomography images at different conductive phase saturations. We then simulate two-phase flow at different Capillary numbers and wettabilities to investigate deviations in resistivity index. We discover that other than water saturation the connectivity of water quantified by Euler characteristic is an important parameter in determining electrical resistivity for intermediate to purely oil-wet conditions. Deviations in electrical resistivity are found to start at low Capillary number (Ca $\sim 10^{-5}$) for intermediate and oil-wet conditions for the full range of water saturations. We study correlations between resistivity index, saturation, and Euler characteristic by using the Pearson product-moment correlation and a linear regression model. We find a strong correlation between water saturation and resistivity index for the water-wet case while for the intermediate and oil-wet cases a strong correlation between Euler characteristic and resistivity index was observed. The results are explained in terms of percolation theory and a general relationship for resistivity index is proposed for intermediate-wet to oil-wet systems whereby the percolation parameter is normalized Euler characteristic. The findings explain previously observed deviations in resistivity index measurements and allow for a means to predict Euler characteristic from laboratory core-scale experiments using the proposed percolation model.

DOI: 10.1103/PhysRevE.98.043102

I. INTRODUCTION

Electrical well logging techniques were originally devised as a way to locate hydrocarbon zones in petroleum reservoirs [1]. Electrical resistivity measurements are also widely used in soil science to measure water saturations in the vadose zone [2] or hydrology to identify the water table [3]. Standard methods of correlating water saturation in clay-free reservoirs to electrical resistivity are based on Archie's law [1]:

$$R_i = \frac{R_t}{R_o} = {S_w}^{-n}, \tag{1}$$

where the resistivity index (R_i) is equal to the ratio of the sample resistivity (R_t) at conductive fluid saturation to the resistivity of the sample at 100% conductive fluid saturation (R_o). Typically the conductive fluid is water and thus, saturation is denoted as S_w. The resistivity index is related to the sample saturation S_w and saturation exponent n. The saturation exponent is determined by fitting Eq. (1) to experimental data. It is commonly accepted that exponent values of ~ 1.5 correspond to water-wet cores while values of ~ 1.9 are for intermediate-wet cores and values from 2.0–25 correspond to oil-wet cores [4–7].

Deviations from Archie's law are often encountered during well logging and laboratory experiments [8,9]. Moss *et al.* [8] found that resistivity index was dependent on flow history and rock wettability using laboratory experiments. Man and Jing [10] discovered similar trends of deviation using pore-network modeling. Yanici *et al.* [11] accounted deviations in resistivity index measurements to the existence of thin water films that exist on rock grains, which provide electrical conductivity at low wetting phase saturation. In addition, Farid *et al.* [12] investigated the stress dependence of resistivity index in sandstone rock using experimental and numerical methods. While these studies identified history dependent variability on resistivity measurements none of these studies explored if nor how fluid morphology in the pore space influenced R_i measurements.

Armstrong *et al.* [13] demonstrated that it was the underlying phase morphology that determined macro-scale properties, such as relative permeability. Differences in flow history, Capillary number, and rock wettability can contribute to different fluid morphologies at constant saturation, which influence macroscale properties such as non-wetting phase relative permeability [14]. Han *et al.* [15] used the random walk method to examine the effect of pore connectivity on resistivity index, they demonstrated that electrical properties are strongly affected by wetting films on the rock surface. Li *et al.* [16] simulated drainage and imbibition using a pore network model and found that R_i is highly dependent on fluid connectivity, which they measured using Bond number and Euler characteristic. With recent developments in x-ray microcomputed tomography (micro-CT), it is now possible to obtain two-phase flow configurations at micrometer resolution within reservoir rocks [17–19] and thus, directly assess how

*ryan.armstrong@unsw.edu.au

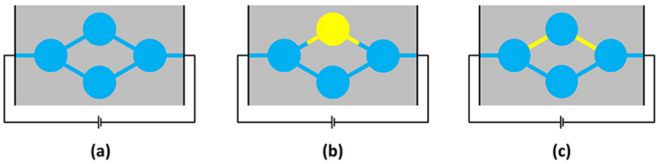

FIG. 1. Resistivity model of a core with different fluid arrangements, blue is the conductive phase (brine) and yellow is the non-conductive phase (oil).

fluid morphology impacts macroscale properties, such as electrical resistivity [20]. Numerical simulation methods are also available to resolve the time gaps between sequential micro-CT scan intervals and to simulate pore-scale flow processes, such as ganglion flow, snap-off and/or dynamic connectivity [13,21–25]. These new techniques provide significant insights into the behavior of pore-scale flow and provide a means to assess rock properties from pore-scale to core-scale.

The Euler characteristic belongs to the Minkowski functionals (MF), which together are able to morphologically describe any 3D object [26,27]. The MF provide a natural mechanism to characterize complex fluid arrangements in porous media because they can provide macroscale values that describes the pore scale geometry and connectivity of fluids. For any three-dimensional space four unique MF exist [27]. The first MF is total volume, which is already accounted for in Archie's law as phase saturation. The second and third MF are surface area and total mean curvature, which have relevance to other pore-scale processes, such as capillary pressure [28,29]. The fourth MF is total Gaussian curvature, which is related to the Euler characteristic through the Gauss-Bonnet theorem [27]. The Euler characteristic is a topological invariant that characterizes the microscale arrangement of objects in a macroscale way [14,30,31]. As seen in percolation and effective medium theories [27,32,33], the macroscale arrangement of phases has a direct influence on effective properties and thus, Euler characteristic is a convenient means to characterize the macroscale state of a system.

Other works have used Euler characteristic to characterize porous media morphology [34], relative permeability [13,14], and absolute permeability [35,36]. Herein, we expand on these works by using Euler characteristic measurements to study electrical resistivity. For instance in Fig. 1, a voltage drop is applied over a simple pore network to measure resistivity. In Fig. 1(a), the pore network is fully saturated with water (electrically conductive phase), which has an Euler characteristic of 0. In Fig. 1(b), water is the wetting phase and an oil ganglion is trapped in the top pore. Here the water has an Euler characteristic of 1. Conversely, in Fig. 1(c), water is the non-wetting phase with an Euler characteristic of 2. These scenarios illustrate the influence that wettability can have on phase connectivity. In particular, a small difference in saturation when water is the non-wetting phase can significantly influence connectivity and thus, the equivalent circuit through which electrical current flows. We explore these scenarios by measuring the Euler characteristic of the electrically conductive phase in a simple porous system with varying degrees of saturation and wettability to study the influence of phase topology on electrical resistivity.

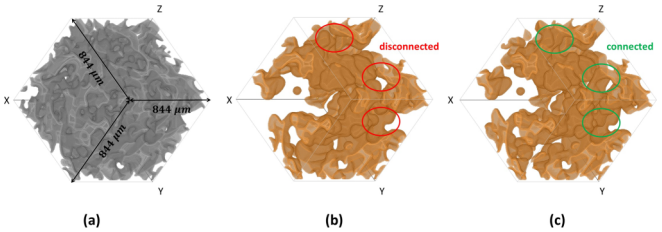

FIG. 2. (a) A 3D rendering of pore space from a $200 \times 200 \times 200$ subset of Robuglass, (b) the conductive phase at $\mathrm{Ca} = 3.1 \times 10^{-6}$ for the 100% oil-wet condition and (c) the conductive phase at $\mathrm{Ca} = 1.1 \times 10^{0}$ for the 100% oil-wet condition. Fluid connectivity changes with Ca as seen with red and green circles in (b) and (c).

II. MATERIALS AND METHODS

A. Simulations and experiments

Two-phase flow is simulated using a parallel implementation of the color-gradient lattice Boltzmann method [37]. The implementation relies on the coupled solution of lattice Boltzmann equations (LBEs) constructed to model the mass and momentum transport. A three-dimensional, 19 velocity (D3Q19) lattice structure and multi-relaxation time (MRT) collision operator are used to model the momentum transport and account for interfacial stresses. Mass transport LBEs rely on a seven-velocity lattice structure (D3Q7) to track the interface between fluids, which is able to accurately model the movement of interfaces and common curves within porous media [38,39]. Simulations performed using the approach demonstrate good agreement with experimental data for the set of three-dimensional fast micro-CT experiments reported herein [13]. The input phase configurations for numerical simulation are synchrotron-based micro-CT data from the TOMCAT bealmine (Paul Scherrer Institute, Swiss Light Source). The images were collected during fractional flow experiments that are explained in Armstrong *et al.* [40]. The porous media used for experiments and numerical simulations is Robuglass, detailed properties of which are provided in [41]. For the experiments, wetting phase is brine and non-wetting phase is n-decane, which are co-injected into the Robuglass sample. The image has a domain size of $990 \times 990 \times 575$ and the resolution is 4.22 μm. The Robuglass core is a cylinder that is tangent to the image boundary, the subset of the pore space that is used for numerical simulation can be seen in Fig. 2(a). The experimental data was used to provide initial conditions for simulation based on the observed fluid distributions. Steady-state flow at constant saturation was simulated by using an external body force in conjunction with fully-periodic boundary conditions. For each observed configuration, the contact angle and Capillary number were varied to explore the resulting geometric changes in fluids. Steady conditions were considered to be achieved once stable values were obtained for the total mass flux for both fluids.

Micro-CT images at different saturations were used as inputs for numerical simulation. The input images are fully water-wet; however, in numerical simulation we can modify the wettability. Wettability is controlled by changing the contact angle, which at equilibrium relates to various surface

energies in the two-fluid system:

$$\cos\theta = \frac{\gamma_{ns} - \gamma_{ws}}{\gamma_{nw}}, \tag{2}$$

where θ is contact angle, γ_{ns} is surface tension between non-wetting and solid phases, γ_{ws} is surface tension between wetting and solid phases, and γ_{nw} is interfacial tension between non-wetting and wetting phases. Herein, the wettability condition is set to be 100% water-wet, 50% water-wet, 50% oil-wet, and 100% oil-wet (purely oil-wet). For example, 100% water-wet is the wettability when $\cos\theta = 1$, which is purely water-wet; 50% water-wet is the wettability when $\cos\theta = 0.5$, which is intermediate water-wet; 50% oil-wet is the wettability when $\cos\theta = -0.5$, which is intermediate oil-wet; 100% oil-wet is the wettability when $\cos\theta = -1$, which is purely oil-wet. Different wettability conditions were chosen since many oil reservoirs are oil and/or intermediate-wet in addition to water-wet [42]. For each saturation, we also simulate two-phase flow at different Capillary number (Ca), which is the ratio of viscous forces to capillary forces, defined as

$$\mathrm{Ca} = \frac{\mu_w v_w}{\gamma_{nw}}, \tag{3}$$

where μ_w is the viscosity of wetting phase and v_w is the average velocity of the wetting phase, which is determined as the integral of the momentum density divided by the integral of mass density. The density ratio and viscosity ratio of wetting phase and non-wetting phase in the simulations are set to be 1, which are close to the ratios between brine and n-decane. The simulation uses periodic boundary conditions and thus, saturation is constant for a given Ca simulation. In Figs. 2(b) and2(c) we provide an example for two different Capillary number simulation results that are at constant non-wetting phase saturation ($S_{nw} = 0.52$). The simulation results are in accordance with previous experimental studies, i.e., increasing Ca results in increased connectivity of non-wetting phase [13,43]. In addition, note that to maintain constant wettability with different interfacial tensions, the surface tension of the oil-solid and water-solid was adjusted accordingly, i.e., when we change γ_{nw}, the contact angle keeps constant as long as we also make a proportionate increase for $\gamma_{ns} - \gamma_{ws}$.

The electrical conductivity of the phase distributions obtained from LB simulations are determined by following the work of Garboczi [44]. For a given fluid with uniform conductivity, the electrical conductivity can be solved by the Laplace equation:

$$\nabla^2\Phi = 0, \tag{4}$$

where Φ is the electrical potential. The Laplace equation was solved using a finite element method applied directly to pore-scale images obtained by LB simulation. Details of the numerical method are reported by Garboczi [44] and Arns *et al.* [45]. The porous system used consisted of three phases: non-conductive glass, electrically conductive water, and non-conductive hydrocarbon. Clay/mineral phase that contains electrically conductive water at low saturation is not considered. Also, thin films along the grain surfaces at irreducible water saturation are likely not fully resolved by the model in addition to thin films developing from flow dynamics [46]. For intermediate to high water saturation, the proportion of the cross sectional area for electrical current to flow attributed to thin films is small in comparison to the connected pathways, which is observed from pore-scale images.

B. Euler characteristic

We use the Minkowski functionals as described by Sakellariou *et al.* [47] to measure the Euler characteristic of phases in pore-scale images. In Fig. 2, we provide an example image of the pore space (a) and the spatial arrangement of less-connected (b) and more-connected (c) non-wetting phase at the same saturation. Here the Euler characteristic of Fig. 2(b) is -6 while in Fig. 2(c) it is -8. In general, highly connected objects will have a more negative Euler characteristic than less connected objects. Assuming that at partial saturation a given phase does not contain any additional connectivity than that present at 100% saturation then the Euler characteristic of a given phase at 100% saturation will represent the maximum possible negative value. Following this rationalization the water Euler characteristic (χ_w) at any partial saturation can be normalized by the Euler characteristic of the entire pore space (χ_p). This normalization approach results in a connectivity metric with presumably a maximum value of 1, a percolation threshold at 0, and highly disconnected objects with negative values. This normalization approach has been shown to be useful for the comparisons of phase connectivity in different rock structures [26,48,49] and is the approach used in this study.

When measuring the Euler characteristic from pore-scale images the pragmatic issue of image resolution should be addressed [50–54]. Due to image resolution error, Euler characteristic of the wetting phase can be difficult to measure since it remains within crevices and corners of the media [14] and may appear disconnected in images. Conversely, non-wetting phase is often within the larger regions of the pore space and thus, resolution error is usually not an issue resulting in straight forward topological characterization. Consequently, Euler characteristic measurements at low wetting phase saturation will have a larger degree of error than measurements at high and/or intermediate saturation. To help circumvent this issue and other issues resulting from isolated pixels due to image segmentation error, phase clusters with a total volume less than 100 voxels are recognized as noise and are removed from our analysis. The total volume of 100 voxels in terms of a sphere corresponds to a structural radius of 12 μm, which is smaller than the average pore size of Robuglass [41].

III. RESULTS AND DISCUSSION

In Fig. 3, we plot resistivity index R_i versus water saturation (S_w) at the four simulated wettability conditions. Throughout the analysis water is the electrically conductive phase and subscript w denotes the water phase. Overall, we observe general trends that follow Archie's law where R_i decreases with increasing water saturation. We fit Archie's law to the simulated data and get exponent values of $n = 1.90$, $n = 2.10$, $n = 1.95$, and $n = 1.90$ for 100% water-wet, 50% water-wet, 50% oil-wet, and 100% oil-wet conditions, respectively. These values are within the range of

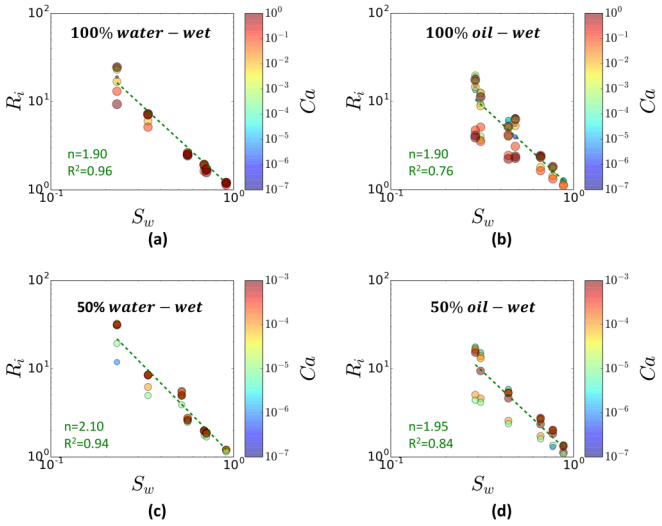

FIG. 3. $R_i - S_w$ curve: data points of different size and color correspond to different Ca at (a) 100% water-wet condition, (b) 100% oil-wet condition, (c) 50% water-wet condition, and (d) 50% oil-wet condition. The dashed line is the power-law fit of function $R_i = S_w^n$.

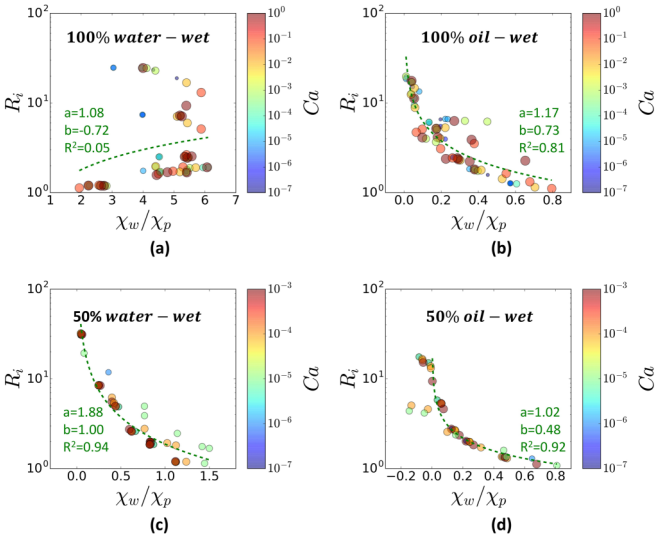

FIG. 4. $R_i - \chi_w/\chi_p$ curve: data points of different size and color correspond to different Ca at (a) 100% water-wet condition, (b) 100% oil-wet condition, (c) 50% water-wet condition, and (d) 50% oil-wet condition. The dashed line is the power-law fit of function $R_i = a(\chi_w/\chi_p)^b$, where a is a proportionality constant and b is the scaling exponent.

expected exponent values for Archie's law [5]. However, the R^2 values for the 50% oil-wet and 100% oil-wet cases are only 0.84 and 0.76, respectively. The poor fit occurs because we observe a range of different R_i values for a single saturation due to changing Capillary number, e.g., see Fig. 3(b). As shown in previous works, Capillary number can directly influence phase topologies [13]. In particular, the topology of the non-wetting phase is influenced by snap-off and coalescence events triggered by changes in Capillary number. It is likely that this type of behavior is seen in the R_i measurements, which will be discussed in detail once the Euler characteristic data are presented.

At 100% water-wet condition, as shown in Fig. 3(a), no R_i deviation is observed at middle to high water saturation ($S_w \geqslant 52\%$). The only deviation occurs at low water saturation where Ca is greater than 10^{-1}. This agrees with experimental results shown by Longeron *et al.* [55] where a strongly water-wet system had very little hysteresis at different flow conditions. At 50% water-wet condition, R_i starts to deviate for midrange water saturations ($S_w < 71\%$) when Ca is greater than 10^{-3}, as shown in Fig. 3(c). At 50% oil-wet condition, the deviations occur over the entire range of water saturations and R_i starts to deviate when Ca is greater than $\sim 10^{-5}$, as shown in Fig. 3(d). At 100% oil-wet condition, deviation occurs for all saturations. However, deviations only start to occur when Ca is greater than 10^{-2}. Amongst all four wettability conditions, the 50% oil-wet condition has deviations occurring over the entire range of saturations and at the lowest Capillary number. Assuming that R_i is influenced by the topology of the electrically conductive phase then the results suggest that phase topologies are more easily manipulated by viscous forces under intermediate wet conditions than 100% water-wet or oil-wet conditions, as supported by recent experimental work [56]. Further support of this is given by the fact that it requires less energy to move the contact line at intermediate wet conditions since the difference in surface energies, γ_{ns} and γ_{ws}, is smaller relative to γ_{wn}. Whereas the topology of water under water-wet conditions is not easily manipulated since it wets the grain surfaces and remains connected over most (if not all) saturations.

Here, we explore the assumption that R_i is influenced by the topology of the electrically conductive phase. In Fig. 4, we plot resistivity index R_i vs. normalized Euler characteristic of water at all four wettability conditions and all Capillary numbers. Remember that the Euler characteristic of water χ_w is normalized by the Euler characteristic of the pore space χ_p [48]. In this study, at 100% water-wet condition, as shown in Fig. 4(a), χ_w/χ_p is in the range of 2 to 7 meaning that water remains highly connected for all of the simulated conditions. It appears that the normalization approach used is not really practical for 100% water-wet conditions since water covers the grain surfaces at partial saturations resulting in higher connectivity than that present at 100% water saturation. The large Euler characteristic can be explained with the 2D simplified model and 3D renderings shown in Fig. 5. At intermediate saturation, shown as Figs. 5(b) and 5(d), a large Euler characteristic is possible because water remains in the corners, which form lots of little loops in the system. More little loops can form at partial saturation compared to the number of loops at 100% saturation resulting in an Euler characteristic greater than 1 for the partial saturation case. In a given pore, at partial saturation, several interlocking loops can exist, as seen in the provided figures.

We also find that χ_w/χ_p does not scale with R_i for the 100% water-wet condition. This is likely because scaling of Euler characteristic to effective medium properties is expected to occur near percolation thresholds, as shown when comparing the Euler characteristic of random porous structures to absolute permeability [36,57]. Since water remains highly connected in the porous media over all saturation

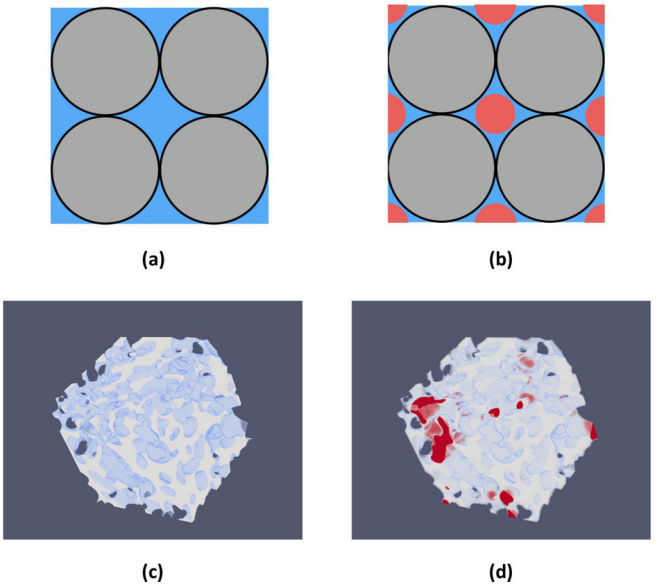

FIG. 5. Comparison between fully saturated and partially saturated porous system. (a) 2D simplified model (solid phase consists of four grains) of fully water saturated porous media at 100% water-wet condition, (b) 2D simplified model of partially saturated porous media (oil trapped in four grains) at 100% water-wet condition, (c) 3D rendering of fully water saturated Robuglass, $\chi_w = \chi_p = -257$, (d) 3D rendering of partially water saturated Robuglass, $\chi_w = -1283$. 3D image size is 200^3.

values, the system does not approach the percolation threshold (for the tested conditions) and thus, addition and/or removal of a few connectivities does not influence the overall R_i. In contrast, we observe a relationship between Euler characteristic and R_i for the other wettability conditions, where χ_{nw}/χ_p is within the range of 0 to 1.

We observe trends between Euler characteristic and R_i for the 50% water-wet, 50% oil-wet, and 100% oil-wet data. All of these data have χ_w/χ_p values within the range of 0 to 1 meaning that water is never more connected than the pore space. Furthermore R_i values tend to rapidly increase as χ_w/χ_p approaches zero, which is near the percolation threshold for water [34,58]. For the 50% oil-wet case, a few of the χ_w/χ_p values are negative meaning that the electrically conductive phase is highly disconnected. However, a percolation test conducted on water demonstrated that a portion of it remained connected across the simulation domain. A negative value can occur when water has many disconnected clusters in addition to a small connected pathway. The transition of χ_w/χ_p from positive to negative is only an estimate of the percolation threshold and thus, does not measure the exact saturation at which percolation ceases [58]. The overall influence of χ_w/χ_p transitioning from a positive to negative value can be observed in Fig. 4 whereby R_i measurements approach infinity near $\chi_w/\chi_p = 0$, which would be expected when water no longer percolates [34].

Here, we use the Pearson product-moment correlation to further understand the relationships between resistivity index, saturation, and Euler characteristic. This correlation matrix is commonly used to examine the strength of association between variables [59]. The Pearson correlation coefficient ranges from -1 to 1, where 1 is total positive correlation, 0 is no correlation, and -1 is total inverse correlation. In Table I, at 100% water-wet condition, the correlation coefficient between $\log(R_i)$ and $\log(S_w)$ is 0.98 and the correlation coefficient between $\log(R_i)$ and $\log(\chi_w/\chi_p)$ is 0.22. These results indicate that for 100% water-wet conditions, water remains well connected and thus, R_i is dominated by S_w. However, for the 100% oil-wet condition, the correlation coefficient between $\log(R_i)$ and $\log(\chi_w/\chi_p)$ is 0.90 while the correlation coefficient between $\log(R_i)$ and $\log(S_w)$ is 0.82. These results demonstrate that a stronger correlation exists between R_i and χ_w than S_w for the 100% oil-wet condition. The correlation between R_i and χ_w becomes even stronger for intermediate wet-conditions while the correlation between R_i and S_w becomes weaker. This suggests that in addition to saturation the Euler characteristic of the electrically conductive phase should be considered when evaluating R_i measurements on rocks that are not 100% water-wet. This also suggests that previously observed deviations from Archie's law could be the result of phase topological changes that can occur at constant saturation. As observed in Fig. 3 different R_i measurements are possible for the same saturation. As proposed in our initial pore network example, a small change in wetting phase saturation can significantly influence non-wetting phase connectivity (Fig. 1).

By using the ordinary least square (OLS) method [60], we can analyze the dependent element R_i in terms of its presumably independent elements S_w and χ_w. Here, we propose three possible linear regression models: $R_i = f(S_w)$, $R_i = f(\chi_w)$, and $R_i = f(S_w, \chi_w)$. To assess the quality of these models, we report the R^2 of each model in Table II. For the 100% water-wet case the addition of χ_w does not improve the estimation of R_i. In fact, R^2 actually deceases when χ_w is considered as the only independent element. This suggests

TABLE I. Correlation coefficients of $\log(R_i) \sim \log(S_w)$ and $\log(R_i) \sim \log(\chi_w/\chi_p)$ at 100% water-wet condition, 100% oil-wet condition, 50% water-wet condition, and 50% oil-wet condition.

Wettability	$\log(R_i) \sim \log(S_w)$	$\log(R_i) \sim \log(\chi_w/\chi_p)$
100% water-wet	0.98	0.22
50% water-wet	0.97	0.97
50% oil-wet	0.88	0.96
100% oil-wet	0.82	0.90

TABLE II. R^2 of $R_i = f(S_w)$, $R_i = f(\chi_w)$, and $R_i = f(S_w, \chi_w)$ model at 100% water-wet condition, 100% oil-wet condition, 50% water-wet condition, and 50% oil-wet condition.

Wettability	$R_i = f(S_w)$	$R_i = f(\chi_w)$	$R_i = f(S_w, \chi_w)$
100% water-wet	0.97	0.05	0.97
50% water-wet	0.95	0.94	0.99
50% oil-wet	0.84	0.92	0.95
100% oil-wet	0.76	0.81	0.88

that saturation alone is able to characterize R_i for water-wet rock. This occurs because water remains connected over the grain surfaces and thus, as saturation increase only the cross-sectional area over which the electrical current can flow increases and thus, saturation alone is able to characterize R_i. This is further supported by the data in Table I where the Pearson correlation coefficient between saturation and topology is 0.32, which demonstrates a weak correlation. For the 50% water-wet case, there is relatively no difference in R^2 if S_w or χ_w are used as the only independent element. However, if both parameters are considered as independent elements then the R^2 increases to 0.99. For the 50% and 100% oil-wet cases, we observe that χ_w as the only independent element provides a better model than when saturation alone is considered. In addition, when both S_w and χ_w are considered as independent elements the R^2 value improves.

Traditionally, the saturation exponent n from Archie's law is used to account for rock wettability. Our data questions this approach since we observe that a single exponent of n is not able to characterize R_i under different wettability conditions when phase topologies are influenced by Capillary number. This occurs because a large range of different phase topologies are possible for the same saturation. For example in Fig. 3, we observed that a range of different R_i values are possible for the same saturation due to different Capillary numbers for the intermediate and oil-wet cases. In addition in Table I, the Pearson correlation coefficient between saturation and topology is greater than 0.72 for the intermediate and oil-wet cases. These results suggests that when saturation increases not only does the cross-sectional area over which the electrical current can flow increases but also the connectivity of the circuit plays a major role when dealing with intermediate and oil-wet systems.

The behavior of a phase transition is well known and is often characterized by percolation theory [61]. Here, critical behavior occurs where an observable parameter (ξ) exhibits a non-polynomial singular dependence on a percolation parameter p. The general relationship is

$$\xi \sim (p - p_c)^{\beta}, \tag{5}$$

where p_c is the percolation parameter at which a system (or network) is no longer connected [61]. Common observable parameters are free energy, finite cluster size, connectedness length, permeability, resistivity, or relative permeability. The Bernab-Li-Maineult (BLM) model [16] utilizes this concept to propose that formation factor is proportional to $(z - z_c)$, where z is the coordination number or a porous network and z_c is the critical value at the percolation threshold. For two-phase flow, percolation models have proposed relative permeability as being proportional to $(s_w - s_{wc})$, where s_{wc} is the critical saturation at which a given phase first spans the entire network [62,63]. As observed in our data, water remains mostly connected with a high degree of connectivity for the 100% water-wet case. In this case, we observe nearly ideal Archie-like behavior where the critical behavior depends on the single percolation parameter of saturation with a critical saturation near zero. For the 50% water-wet cases, we observe similar behavior where the single percolation parameter of saturation is sufficient to characterize the behavior of R_i. However, alternatively, we also find that χ_w/χ_p can be a suitable percolation parameter. Here, a normalized Euler characteristic of zero estimates the percolation threshold. For the 100% and 50% oil-wet cases, we find χ_w/χ_p to be a well suited percolation parameter where the critical point at which percolation ceases is naturally captured by $\chi_w/\chi_p = 0$. Near this threshold, R_i scales with Euler characteristic as observed in Tables I, II, and Fig. 4. From these finding, we propose the following relationship for intermediate to oil-wet systems:

$$R_i \sim \left(\frac{\chi_w}{\chi_p}\right)^b, \tag{6}$$

where b is the scaling exponent.

According to Eq. (6), for well logging and experimental studies, R_i measurements can provide insight into phase connectivity when a rock is known to be oil (or intermediate) wet. In addition, the proposed relationship provides the opportunity for new experimental approaches to study multiphase flow. Numerous studies regarding ganglion dynamics and phase connectivity during two-phase immiscible flow are available in the literature [17,18,40,64,65]. Our results suggest that conductivity measurements during fractional flow experiments where the electrically conductive phase is intermediate or non-wetting would provide a means to predict non-wetting phase connectivity during fractional flow. This would provide a pragmatic way to link pore-scale properties to macroscale behavior and to test emerging theories on multi-phase flow that consider phase connectivity [29,66–68]. Overall, insights into how Capillary number influences phase connectivity and resulting hysteresis effects could be studied at the macro-scale with simple electrical conductivity measurements.

IV. CONCLUSIONS

We simulated two-phase flow under different Capillary numbers and wettabilities using the lattice Boltzmann method. We then used the finite element method to determine the resistivity index for each simulated case and characterized connectivity by measuring the Euler characteristic of water. The main results are: (1) different R_i values are possible for the same saturation, (2) electrical conductivity is highly dependent on phase connectivity for intermediate to oil-wet conditions, (3) water saturation is a suitable critical parameter for determining R_i under water-wet conditions, and (4) normalized Euler characteristic is a suitable critical parameter for determining R_i under oil-wet (or intermediate-wet) conditions. Overall, this work provides a means to characterize pore-scale water connectivity in terms of Euler characteristic for intermediate to oil-wet conditions by electrical resistivity measurements. These insights help to explain why dependencies have been seen in previous R_i measurements that only consider phase saturation in particular for reservoir rocks, which are not always 100% water wet.

ACKNOWLEDGMENTS

This work was supported by an award of computer time provided by the Department of Energy INCITE program. This research also used resources of the Oak Ridge Leadership Computing Facility, which is a DOE Office of Sci-

ence User Facility supported under Contract No. DE-AC05-00OR22725. X-ray microcomputed tomography was performed on the TOMCAT beamline at the Swiss Light Source, Paul Scherrer Institute, Villigen, Switzerland.

[1] G. E. Archie *et al.*, Transactions of the AIME **146**, 54 (1942).
[2] A. Samouëlian, I. Cousin, A. Tabbagh, A. Bruand, and G. Richard, Soil Tillage Res. **83**, 173 (2005).
[3] A. K. Benson, K. L. Payne, and M. A. Stubben, Geophysics **62**, 80 (1997).
[4] S. Sweeney and H. Jennings, Jr., J. Phys. Chem. **64**, 551 (1960).
[5] W. B. Morgan, S. J. Pirson *et al.*, *SPWLA 5th Annual Logging Symposium* (Society of Petrophysicists and Well-Log Analysts, Midland, Texas, 1964).
[6] M. G. Lewis, M. M. Sharma, H. F. Dunlap *et al.*, *SPWLA 29th Annual Logging Symposium* (Society of Petrophysicists and Well-Log Analysts, San Antonio, Texas, 1988).
[7] W. Jun-Zhi, O. B. Lile *et al.*, SPE Form. Eval. **6**, 470 (1991).
[8] A. Moss, X. Jing, and J. Archer, J. Pet. Sci. Eng. **24**, 231 (1999).
[9] M. A. Knackstedt, C. H. Arns, A. P. Sheppard, T. J. Senden, R. M. Sok, Y. Cinar, A. O. Olafuyi, W. V. Pinczewski, G. Padhy, and M. Ioannidis, Pore scale analysis of electrical resistivity on complex core material, *International Symposium of the Society of Core Analysts, SCA2007-33, Calgary, Canada* (Society of Core Analysts, 2007).
[10] H. Man and X. Jing, J. Pet. Sci. Eng. **24**, 255 (1999).
[11] S. Yanici, J.-Y. Arns, Y. Cinar, W. Pinczewski, and C. Arns, Transp. Porous Media **96**, 457 (2012).
[12] M. Farid, J.-Y. Arns, W. Pinczewski, C. Arns *et al.*, SPE Annual Technical Conference and Exhibition (Society of Petroleum Engineers, Dubai, UAE, 2016).
[13] R. T. Armstrong, J. E. McClure, M. A. Berrill, M. Rücker, S. Schlüter, and S. Berg, Phys. Rev. E **94**, 043113 (2016).
[14] Z. Liu, A. Herring, C. Arns, S. Berg, and R. T. Armstrong, Transp. Porous Media **118**, 99 (2017).
[15] M. Han, S. Youssef, E. Rosenberg, M. Fleury, and P. Levitz, Phys. Rev. E **79**, 031127 (2009).
[16] M. Li, Y. Tang, Y. Bernabé, J. Zhao, X. Li, X. Bai, and L. Zhang, J. Geophys. Res.: Solid Earth **120**, 4055 (2015).
[17] S. Berg, H. Ott, S. A. Klapp, A. Schwing, R. Neiteler, N. Brussee, A. Makurat, L. Leu, F. Enzmann, J.-O. Schwarz *et al.*, Proc. Natl. Acad. Sci. **110**, 3755 (2013).
[18] H. H. Khanamiri, O. Torsæter, and G. J. Voss, *International Symposium of the Society of Core Analysts, Vienna, Austraia* (The Society of Core Analysts, Vienna, Austria, 2017).
[19] C. Garing, J. A. de Chalendar, M. Voltolini, J. B. Ajo-Franklin, and S. M. Benson, Adv. Water Resour. **104**, 223 (2017).
[20] C. H. Arns, M. A. Knackstedt, M. V. Pinczewski, and W. Lindquist, Geophys. Res. Lett. **28**, 3361 (2001).
[21] L. Chen, Q. Kang, Y. Mu, Y.-L. He, and W.-Q. Tao, Int. J. Heat Mass Transf. **76**, 210 (2014).
[22] R. Armstrong, S. Berg, O. Dinariev, N. Evseev, D. Klemin, D. Koroteev, and S. Safonov, Transp. Porous Media **112**, 577 (2016).
[23] C. A. Reynolds, H. Menke, M. Andrew, M. J. Blunt, and S. Krevor, Proc. Natl. Acad. Sci. **114**, 8187 (2017).
[24] Y. Chen, Y. Li, A. J. Valocchi, and K. T. Christensen, J. Contam. Hydrol. **212**, 14 (2017).
[25] J. O. Helland, H. A. Friis, E. Jettestuen, and S. M. Skjæveland, Geophys. Res. Lett. **44**, 4933 (2017).
[26] S. Schlüter, S. Berg, M. Rücker, R. Armstrong, H.-J. Vogel, R. Hilfer, and D. Wildenschild, Water Resour. Res. **52**, 2194 (2016).
[27] K. R. Mecke, *Statistical Physics and Spatial Statistics* (Springer, Berlin, 2000), pp. 111–184.
[28] R. T. Armstrong, M. L. Porter, and D. Wildenschild, Adv. Water Resour. **46**, 55 (2012).
[29] J. E. McClure, R. T. Armstrong, M. A. Berrill, S. Schlüter, S. Berg, W. G. Gray, and C. T. Miller, Phys. Rev. Fluids **3**, 084306 (2018).
[30] Y. Gao, Q. Lin, B. Bijeljic, and M. J. Blunt, Water Resour. Res. **53**, 10274 (2017).
[31] Y. Jing, R. T. Armstrong, H. L. Ramandi, and P. Mostaghimi, J. Geophys. Res.: Solid Earth **122**, 9849 (2017).
[32] R. Hilfer, Phys. Rev. B **44**, 60 (1991).
[33] A. Hunt, R. Ewing, and B. Ghanbarian, *Percolation Theory for Flow in Porous Media*, 3rd ed. (Springer, 2014).
[34] H.-J. Vogel, U. Weller, and S. Schlüter, Comput. Geosci. **36**, 1236 (2010).
[35] Z. Liu, A. Herring, V. Robins, and R. Armstrong, *International Symposium of the Society of Core Analysts, Vienna, Austraia* (The Society of Core Analysts, Vienna, Austria, 2017).
[36] C. Scholz, F. Wirner, J. Götz, U. Rüde, G. E. Schröder-Turk, K. Mecke, and C. Bechinger, Phys. Rev. Lett. **109**, 264504 (2012).
[37] J. E. McClure, H. Wang, J. F. Prins, C. T. Miller, and W. Feng, *28th IEEE International Parallel and Distributed Processing Symposium* (APS, Phoenix, AZ, 2014), pp. 583–592.
[38] J. E. McClure, J. F. Prins, and C. T. Miller, Comput. Phys. Commun. **185**, 1865 (2014).
[39] J. E. McClure, M. A. Berrill, W. G. Gray, and C. T. Miller, J. Fluid Mech. **796**, 211 (2016).
[40] R. T. Armstrong, H. Ott, A. Georgiadis, M. Rücker, A. Schwing, and S. Berg, Water Resour. Res. **50**, 9162 (2014).
[41] S. Berg, R. Armstrong, H. Ott, A. Georgiadis, S. Klapp, A. Schwing, R. Neiteler, N. Brussee, A. Makurat, L. Leu *et al.*, Petrophysics **55**, 304 (2014).
[42] S. Iglauer, M. Fernø, P. Shearing, and M. Blunt, J. Colloid Interface Sci. **375**, 187 (2012).
[43] A. Payatakes, Annu. Rev. Fluid Mech. **14**, 365 (1982).
[44] E. J. Garboczi, *Finite Element and Finite Difference Programs for Computing the Linear Electric and Elastic Properties of Digital Images of Random Materials* (Building and Fire Research Laboratory, National Institute of Standards and Technology, Gaithersburg, MD, 1998).
[45] C. H. Arns, M. A. Knackstedt, and N. S. Martys, Phys. Rev. E **72**, 046304 (2005).
[46] L. Cueto-Felgueroso and R. Juanes, Phys. Rev. Lett. **108**, 144502 (2012).
[47] A. Sakellariou, C. H. Arns, A. P. Sheppard, R. M. Sok, H. Averdunk, A. Limaye, A. C. Jones, T. J. Senden, and M. A. Knackstedt, Materials Today **10**, 44 (2007).
[48] A. L. Herring, E. J. Harper, L. Andersson, A. Sheppard, B. K. Bay, and D. Wildenschild, Adv. Water Resour. **62**, 47 (2013).

[49] A. L. Herring, L. Andersson, S. Schlüter, A. Sheppard, and D. Wildenschild, Adv. Water Resour. **79**, 91 (2015).
[50] C. Lang, J. Ohser, and R. Hilfer, J. Microsc. **203**, 303 (2001).
[51] W. Nagel, J. Ohser, and K. Pischang, J. Microsc. **198**, 54 (2000).
[52] D. Legland, K. Kiêu, and M.-F. Devaux, Image Analysis & Stereology **26**, 83 (2011).
[53] H. Mantz, K. Jacobs, and K. Mecke, J. Stat. Mech.: Theor. Exp. (2008) P12015.
[54] J. Ohser and F. Mücklich, *Statistical Analysis of Microstructures in Materials Science* (Wiley, New York, 2000).
[55] D. Longeron, M. Argaud, J.-P. Feraud *et al.*, SPE Formation Evaluation **4**, 194 (1989).
[56] S. Zou, R. T. Armstrong, J.-Y. Arns, C. H. Arns, and F. Hussain, Water Resour. Res. **54**, 2 (2018).
[57] C. Scholz, F. Wirner, M. A. Klatt, D. Hirneise, G. E. Schröder-Turk, K. Mecke, and C. Bechinger, Phys. Rev. E **92**, 043023 (2015).
[58] V. Robins, M. Saadatfar, O. Delgado-Friedrichs, and A. P. Sheppard, Water Resour. Res. **52**, 315 (2016).
[59] J. Benesty, J. Chen, Y. Huang, and I. Cohen, *Noise Reduction in Speech Processing* (Springer, Berlin, 2009), pp. 1–4.
[60] S. Seabold and J. Perktold, Proc. Python Sci. Conf. **57**, 61 (2010).
[61] M. Sahimi, *Applications of Percolation Theory* (CRC Press, 1994).
[62] M. Blunt, M. J. King, and H. Scher, Phys. Rev. A **46**, 7680 (1992).
[63] R. Larson, L. Scriven, and H. Davis, Chem. Eng. Sci. **36**, 57 (1981).
[64] D. Avraam and A. Payatakes, J. Fluid Mech. **293**, 207 (2006).
[65] K. Mohanty, H. Davis, L. Scriven *et al.*, SPE Reservoir Eng. **2**, 113 (1987).
[66] R. Hilfer, Physica A **359**, 119 (2006).
[67] W. G. Gray and C. T. Miller, Adv. Water Resour. **28**, 161 (2005).
[68] S. Khorsandi, L. Li, R. T. Johns *et al.*, SPE Journal **22**, 1915 (2017).